Paper accepted for presentation at 2009 IEEE Bucharest Power Tech Conference, June 28th - July 2nd, Bucharest, Romania

Multivariable Feedback Design of VSC-HVDC Connected to Weak AC Systems

Lidong Zhang, *Member, IEEE,* and Hans-Peter Nee, *Senior Member, IEEE*

***Abstract*—Power-synchronization control is particularly applicable to voltage-source converters based high-voltage direct-current (HVDC) transmission connected to weak ac systems. In this paper, the multivariable feedback design aspect of the power-synchronization control is investigated by two design approaches: Internal model control (IMC) and $\mathcal{H}_\infty$ control. The paper shows that both of the methods can meet the design requirements and show good robustness with different model uncertainties and load disturbances. The advantage of the IMC approach is that it provides a transparent framework for control-system design and tuning. The algorithm used for the IMC design in this paper is simple, yet it achieves similar or even better performance and robustness compared to the more advanced optimization-based $\mathcal{H}_\infty$ controller.**

***Index Terms*—Control, converters, HVDC, phase-locked loops, power systems, stability.**

I. Introduction

VOLTAGE-SOURCE converter (VSC) based high-voltage direct-current (HVDC) transmission attracted significant attention in recent years [1]. Several control methods have been proposed. Among them, the vector current-control is the most common control scheme [2], [3]. The basic principle of vector current-control is to control the instantaneous active power and reactive power independently through a fast inner current-control loop. Vector current-control has been the most widely used design for almost all grid-connected VSC applications [4].

One of the advantages of VSC-HVDC, compared to the conventional thyristor-based HVDC, is its potential to operate in very weak system connections. However, several investigations have shown that VSC-HVDC based on vector current-control also has problems in maintaining stable operation if the connected ac system is weak [5], [6]. Therefore, a new control method for grid-connected VSCs, i.e., the power-synchronization control, was proposed in [7] to solve the weak-ac-system connection problem. One of the major features of the power-synchronization control is that the VSC synchronizes with the ac system through an active-power control loop, similar to the operation of a synchronous machine. By using power as a way of synchronization, the VSC avoids the instability caused by a standard phase-locked loop (PLL) in a weak ac-system connection [5], [8], [9]. Moreover, a VSC terminal can give the weak ac system strong voltage support, just like a normal synchronous machine does.

L. Zhang is with ABB Power Systems, SE-771 80 Ludvika, Sweden e-mail: lidong.zhang@se.abb.com.

H.-P. Nee is with the School of Electrical Engineering, Royal Institute of Technology, SE-100 44 Stockholm, Sweden e-mail: hansi@ee.kth.se.

978-1-4244-2235-7/09/$25.00 ©2009 IEEE

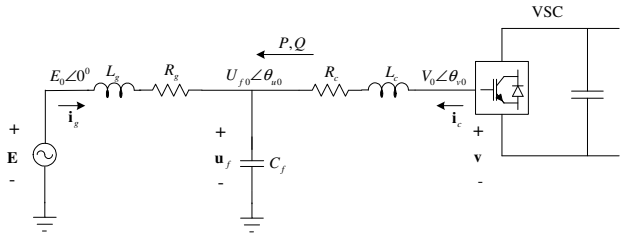

Fig. 1. The main circuit diagram of a VSC converter connected to ac system.

The control of grid-connected VSCs is fundamentally of multi-input multi-output (MIMO) nature, i.e., both the active power and the alternating voltage at the point-of-common-coupling (PCC) are to be controlled. In this paper, the multivariable feedback design aspect of the power-synchronization control is investigated by two design approaches: Internal model control (IMC) and $\mathcal{H}_\infty$ control.

II. VSC-HVDC Connected to Weak AC systems

Fig. 1 shows the main circuit diagram of a VSC-HVDC converter connected to an ac system. L_c and R_c are the inductance and resistance of the phase reactor of the VSC, and L_g and R_g are the inductance and resistance of the ac system. C_f is the ac capacitor connected at the PCC. The bold letter symbols $\mathbf{E}$, $\mathbf{u_f}$, and $\mathbf{v}$ represent the voltage vectors of the ac source, the PCC, and the VSC. E_0, U_{f0}, and V_0, are their corresponding voltage magnitudes. The ac-source is used as the voltage reference, and the load angles of $\mathbf{u_f}$ and $\mathbf{v}$ are θ_{u0} and θ_{v0} respectively. P and Q are the active power and reactive power from the VSC to the ac system. $\mathbf{i}_c$ is the ac-current vector of the phase reactor, and $\mathbf{i}_g$ is the ac-current vector from the ac source.

A. Characteristics of Weak AC Systems

A weak ac system is typically characterized by its high impedance. As the ac-system impedance increases, the voltage magnitude of the ac system will become ever more sensitive to power variations of the HVDC system. This difficulty is usually measured by the short-circuit ratio (SCR), which is a ratio of the ac-system short-circuit capacity vs. the rated power of the HVDC system. SCR is directly related to the ac-system inductance L_g. By neglecting the resistance R_g, and if L_g is expressed in per unit (p.u.) value with line-to-line voltage of the ac system, and the rated power of HVDC system as base value, SCR can be expressed as

$$\mathrm{SCR} = \frac{1}{\omega_1 L_g} \tag{1}$$

where ω_1 is the angular frequency of the ac system. If the frequency of the ac system is assumed to be constant and nominal, i.e., $\omega_1 = 1.0$ p.u., SCR is simply the inverse of L_g.

Besides the voltage-control difficulty, SCR also imposes a theoretical limitation on the maximum power that the HVDC system is able to transmit to or from the ac system. This can be shown by the following well-known power-angle equation

$$P = \frac{|\mathbf{E}||\mathbf{u}_\mathrm{f}|}{\omega_1 L_g} \sin\theta_{u0} \tag{2}$$

i.e., the maximum load angle between the ac-source and the PCC bus of the VSC-HVDC cannot be beyond 90° in steady-state. The VSC-HVDC based on power-synchronization control theoretically is able to maintain operation at load angles very close to 90°. However, in practice, the load angle and the bandwidth of the controller should be limited to ensure a safe stability margin [7].

Low-order-harmonic resonance is another concern for VSC-HVDC connected to weak ac systems. With the increasing ac-system inductance, the resonance frequency between the ac filter of VSC-HVDC (or other large shunt capacitors in the proximity) and the ac-system inductance tends to be lower. Therefore, it is essential for controllers of VSC-HVDC converters to provide damping to those resonant poles.

B. Modelling of VSC Connected to a Weak AC System

In a synchronous reference frame, the dynamic equations of the main circuit in Fig. 1 can be written as

$$\begin{aligned} L_c\frac{d\mathbf{i}_c}{dt} &= \mathbf{v} - \mathbf{u}_f - R_c\mathbf{i}_c - j\omega_1 L_c\mathbf{i}_c \\ C_f\frac{d\mathbf{u}_f}{dt} &= \mathbf{i}_c + \mathbf{i}_g - j\omega_1 C_f\mathbf{u}_f \\ L_g\frac{d\mathbf{i}_g}{dt} &= \mathbf{E} - \mathbf{u}_f - R_g\mathbf{i}_g - j\omega_1 L_g\mathbf{i}_g \end{aligned} \tag{3}$$

and in dq-component form

$$\begin{aligned} L_c\frac{di_{cd}}{dt} &= v_d - u_{fd} - R_c i_{cd} + \omega_1 L_c i_{cq} \\ L_c\frac{di_{cq}}{dt} &= v_q - u_{fq} - R_c i_{cq} - \omega_1 L_c i_{cd} \\ C_f\frac{du_{fd}}{dt} &= i_{cd} + i_{gd} + \omega_1 C_f u_{fq} \\ C_f\frac{du_{fq}}{dt} &= i_{cq} + i_{gq} - \omega_1 C_f u_{fd} \\ L_g\frac{di_{gd}}{dt} &= E_0 - u_{fd} - R_g i_{gd} + \omega_1 L_g i_{gq} \\ L_g\frac{di_{gq}}{dt} &= -u_{fq} - R_g i_{gq} - \omega_1 L_g i_{gd}. \end{aligned} \tag{4}$$

For power-synchronization control, the system is controlled by adjusting the phase angle θ and voltage magnitude V of the VSC output. Thus the real and imaginary parts of the VSC vector v_d and v_q can be expressed as

$$v_d = V\cos\theta \quad v_q = V\sin\theta. \tag{5}$$

The output variables which are of importance for VSC control are the active power P and the voltage magnitude U_f at the PCC. These variables are defined as

$$P = \mathrm{Re}\left\{\mathbf{u}_f\mathbf{i}_c^*\right\} \quad U_f = \sqrt{U_{fd}^2 + U_{fq}^2}. \tag{6}$$

The state-space model can be obtained by linearizing (4), (5), and (6), which yields the following form

$$\begin{aligned} \frac{d}{dt}\mathbf{x} &= A\mathbf{x} + B\mathbf{u} \\ \mathbf{y} &= C\mathbf{x} + D\mathbf{u} \end{aligned} \tag{7}$$

where

$$\begin{aligned} \mathbf{u} &= \begin{bmatrix} \Delta\theta \\ \Delta V/V_0 \end{bmatrix} \mathbf{y} = \begin{bmatrix} \Delta P \\ \Delta U_f \end{bmatrix} \\ \mathbf{x} &= [\Delta i_{cd}, \Delta i_{cq}, \Delta u_{fd}, \Delta u_{fq}, \Delta i_{gd}, \Delta i_{gq}]^T \end{aligned} \tag{8}$$

The state-space representation (7) can also be written in input-output transfer matrix form

$$\mathbf{y}(s) = \left[C\cdot(sI - A)^{-1}\cdot B + D\right]\mathbf{u}(s) \tag{9}$$

which yields

$$\begin{bmatrix} \Delta P \\ \Delta U_f \end{bmatrix} = \underbrace{\begin{bmatrix} J_{\mathrm{P}\theta}(s) & J_{\mathrm{PV}}(s) \\ J_{\mathrm{U}_f\theta}(s) & J_{\mathrm{U}_f\mathrm{V}}(s) \end{bmatrix}}_{J(s)} \cdot \begin{bmatrix} \Delta\theta \\ \Delta V/V_0 \end{bmatrix} \tag{10}$$

C. High-Pass Current Control

In VSC-HVDC applications, the resistance in the system is usually very low. Thus, the resonances in the ac system have to be damped out by the control system. This is especially important for VSC-HVDC connected to weak ac systems, where the low-order harmonic resonance may interact with the control system of the VSC. Therefore, a high-pass current control was proposed in [7] to add "active damping" to the resonant poles. The high-pass current controller has the transfer function

$$H_{\mathrm{HP}}(s) = \frac{k_v s}{\alpha_v + s}. \tag{11}$$

For the convenience of the control design, $H_{\mathrm{HP}}(s)$ is treated as a part of the system model $J(s)$. By including $H_{\mathrm{HP}}(s)$, the dynamic equation of the phase-reactor part (the first dynamic equation) in (3) is modified as

$$L_c\frac{d\mathbf{i_c}}{dt} = \mathbf{v} - H_{\mathrm{HP}}(s)\,\mathbf{i}_c - \mathbf{u}_\mathrm{f} - R_c\mathbf{i}_c - j\omega_1 L_c\mathbf{i}_c. \tag{12}$$

To fit (12) in the state-space form, a new state variable $i_c^{'}$ needs to be introduced. With the new state variable $i_c^{'}$, (12) is expressed as

$$\begin{aligned} L_c\frac{d\mathbf{i}_c}{dt} &= L_c\mathbf{i}_c^{'} + \left(\mathbf{v} - (R_c + k_v + \alpha_v L_c)\,\mathbf{i}_c - \mathbf{u}_\mathrm{f} - j\omega_1 L_c\mathbf{i}_c\right) \\ L_c\frac{d\mathbf{i}_c^{'}}{dt} &= \alpha_v\left(\mathbf{v} - R_c\mathbf{i}_c - \mathbf{u}_\mathrm{f} - j\omega_1 L_c\mathbf{i}_c\right). \end{aligned} \tag{13}$$

Replacing the phase-reactor dynamic equations in (3) by (13) and following the same procedure in Section II-B, the transfer matrix $J(s)$ including $H_{\mathrm{HP}}(s)$ can be obtained. As shown by the pole-zero map of $J(s)$ in Fig. 2, the effect of $H_{\mathrm{HP}}(s)$ is to shift the resonant poles of $J(s)$ towards the left half plane.

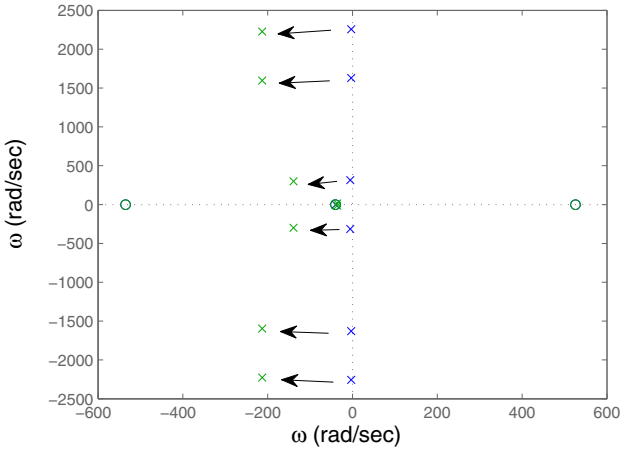

Fig. 2. Damping effect of $H_{\mathrm{HP}}(s)$ on the resonant poles of $J(s)$. Blue: $J(s)$ without $H_{\mathrm{HP}}(s)$, Green: $J(s)$ with $H_{\mathrm{HP}}(s)$. Main circuit parameters: $L_g = 0.667$ p.u. (SCR=1.5), $R_g = 0.01$ p.u., $L_c = 0.2$ p.u., $R_c = 0.01$ p.u., $C_f = 0.17$ p.u.. Initial conditions: $V_0 = 1.05$ p.u., $E_0 = 1.0$ p.u., $\theta_{v0} = 60°$. $H_{\mathrm{HP}}(s)$: $k_v = 0.35$ p.u., $\alpha_v = 40$ rad/sec.

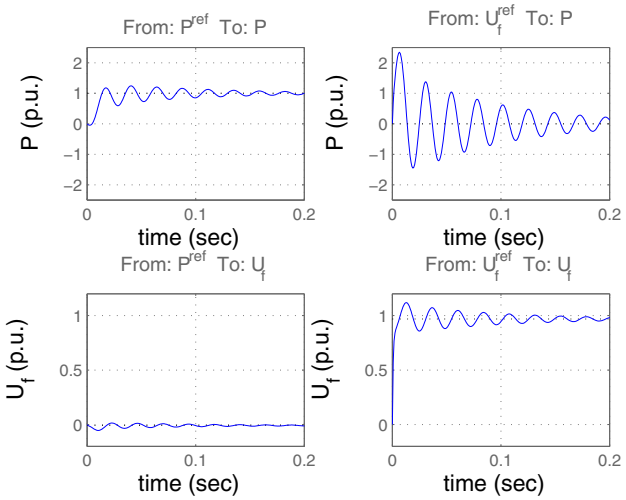

Fig. 3. Active-power P and alternating-voltage U_f step responses with decentralized controllers.

D. Reduced-Order Model

By including the high-pass current control $H_{\mathrm{HP}}(s)$, $J(s)$ becomes 8th order. Such high-order models often lead to high-order controllers, as the controller-design approaches used in this paper are all based on the model $J(s)$. For VSC-HVDC applications, the ac capacitor often has a low value. Therefore, a reduced-order model without the ac capacitor is adopted in this paper for the controller design, while the robustness of the controller with different ac-capacitor sizes is verified by time simulations.

Following the procedure described in [7], the four transfer functions of the transfer matrix $J(s)$ including $H_{\mathrm{HP}}(s)$ can be derived. All the four transfer functions have the general form

$$J_{\mathrm{xx}}(s) = \frac{a_0 s^2 + a_1 s + a_2}{\left(sL + R + H_{\mathrm{HP}}(s)\right)^2 + \left(\omega_1 L\right)^2} \tag{14}$$

where the inductance L and resistance R are defined as

$$L = L_g + L_c \quad R = R_g + R_c \tag{15}$$

and the a-coefficients are listed in Table I, with the k-parameters defined as

$$\begin{aligned} k_1 &= V_0 U_{f0} \cos\left(\theta_{v0} - \theta_{u0}\right) \\ k_2 &= V_0 U_{f0} \sin\left(\theta_{v0} - \theta_{u0}\right) \\ k_3 &= E_0 V_0 \cos\theta_{v0} \\ k_4 &= E_0 V_0 \sin\theta_{v0}. \end{aligned} \tag{16}$$

TABLE I
COEFFICIENTS OF THE TRANSFER FUNCTIONS OF (14)

$J_{\mathrm{P}\theta}(s)$	a_0	$\frac{L}{\omega_1}(k_3 - k_1)$
	a_1	$\frac{(R+H_{\mathrm{HP}}(s))}{\omega_1}(k_3 - k_1) - Lk_2$
	a_2	$\omega_1 L k_3 - (R + H_{\mathrm{HP}}(s))\, k_4$
$J_{\mathrm{U}_f\theta}(s)$	a_0	$-LL_g k_2 / U_{f0}$
	a_1	$-(R + H_{\mathrm{HP}}(s))\, L_g k_2 / U_{f0}$
	a_2	$-\omega_1^2 LL_g k_2 / U_{f0} - (R + H_{\mathrm{HP}}(s))\, L_g k_1 / U_{f0}$
$J_{\mathrm{PV}}(s)$	a_0	$\frac{L}{\omega_1}(k_4 - k_2)$
	a_1	$\frac{(R+H_{\mathrm{HP}}(s))}{\omega_1}(k_4 - k_2) + Lk_1$
	a_2	$\omega_1 L k_4 + (R + H_{\mathrm{HP}}(s))\, k_3$
$J_{\mathrm{U}_f\mathrm{V}}(s)$	a_0	$LL_g k_1 / U_{f0}$
	a_1	$(R + H_{\mathrm{HP}}(s))\, L_g k_1 / U_{f0}$
	a_2	$\omega_1^2 LL_g k_1 / U_{f0} - (R + H_{\mathrm{HP}}(s))\, L_g k_2 / U_{f0}$

III. Multivariable Internal Model Controller Design

Although the individual couplings between the active power and the phase angle of the VSC on the one hand, and the magnitudes of the PCC voltage and the VSC voltage on the other hand are very strong, the interaction between the two channels exists, especially if higher bandwidth of the controller is required. Fig. 3 shows the step responses of the active power P and alternating voltage U_f with decentralized controllers. The plots clearly show the cross-coupling between the two control channels.

A. Controller Design

The concept of IMC design originally came from the idea that the complete system includes the process model explicitly in addition to the controller [10] as shown by the block diagram in Fig. 4. For the application of VSC-HVDC, $r(s) = [P^{\mathrm{ref}},\ U_f^{\mathrm{ref}}]$, $u(s) = [\Delta\theta,\ \Delta V/V_0]$, and $y(s) = [P,\ U_f]$. If the process $J(s)$ is stable and the process model $\widetilde{J}(s)$ is equal to $J(s)$, the whole system is internally stable if and only if $K(s)$ is stable. Thus, if we choose

$$K(s) = \widetilde{J}^{-1}(s)\, F(s) \tag{17}$$

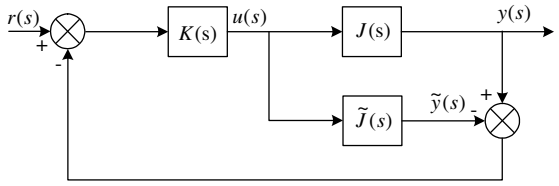

Fig. 4. Block diagram of Internal Model Control system.

the output response would be

$$y(s) = J(s)\,\tilde{J}^{-1}(s)\,F(s)\,r(s) = F(s)\,r(s). \tag{18}$$

Therefore, the closed-loop bandwidth would be solely determined by the filter $F(s)$, which is often defined as a first-order filter with the desired bandwidth. However, in the application of VSC-HVDC, the above philosophy cannot work directly, since the transfer matrix $J(s)$ contains a right-half plane (RHP) zero, as shown in Fig. 2. A direct inverse of $J(s)$ would end up with an unstable controller.

In such a situation, a factorization technique needs to be applied [11]. Consequently, the process model can be factorized into two parts

$$\tilde{J}(s) = \tilde{J}_n(s)\,\tilde{J}_p(s) \tag{19}$$

where $\tilde{J}_n(s)$ contains the invertible elements and $\tilde{J}_p(s)$ contains the non-invertible elements.

An easy factorization method is to place the RHP transmission zero at the diagonal part of $\tilde{J}_p(s)$ as

$$\tilde{J}_p(s) = \begin{bmatrix} \frac{Z_{\mathrm{RHP}}-s}{Z_{\mathrm{RHP}}+s} & 0 \\ 0 & \frac{Z_{\mathrm{RHP}}-s}{Z_{\mathrm{RHP}}+s} \end{bmatrix} \tag{20}$$

where Z_{RHP} is the RHP transmission zero of the transfer matrix $J(s)$. The invertible matrix $\tilde{J}_n(s)$ can be solved by (19) and (20). A low-pass filter matrix $F(s)$ is chosen to specify the closed-loop bandwidth

$$F(s) = \begin{bmatrix} \frac{\alpha_p}{s+\alpha_p} & 0 \\ 0 & \frac{\alpha_u}{s+\alpha_u} \end{bmatrix} \tag{21}$$

where α_p and α_u are the desired bandwidths of the active-power controller and alternating-voltage controllers. In determining the bandwidth α_p and α_u, the RHP transmission zero of $J(s)$ has to be considered. As a rule of thumb, the bandwidth of the closed-loop system should be chosen at least lower than half of the location of the RHP zero [12].

Thus, the controller is designed as

$$K(s) = \tilde{J}_n^{-1}(s)\,F(s). \tag{22}$$

If the model is assumed to be perfect, i.e., $J(s)\,\tilde{J}_n^{-1}(s) = J_p(s)$, then the output response would be

$$y(s) = J_p(s)\,F(s)\,r(s). \tag{23}$$

Because both $J_p(s)$ and $F(s)$ are diagonal, the resulting closed-loop response is also diagonal. As shown by the active-power and alternating-voltage step responses with the linear model in Fig. 6, the IMC controller successfully decouples the cross-coupling between the two control channels.

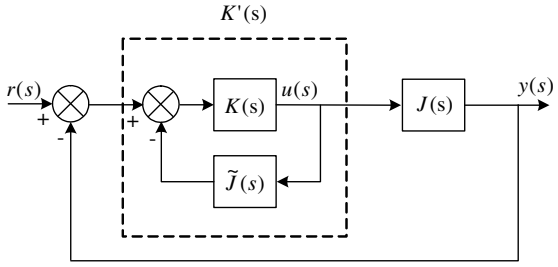

Fig. 5. IMC in classical feedback-control structure.

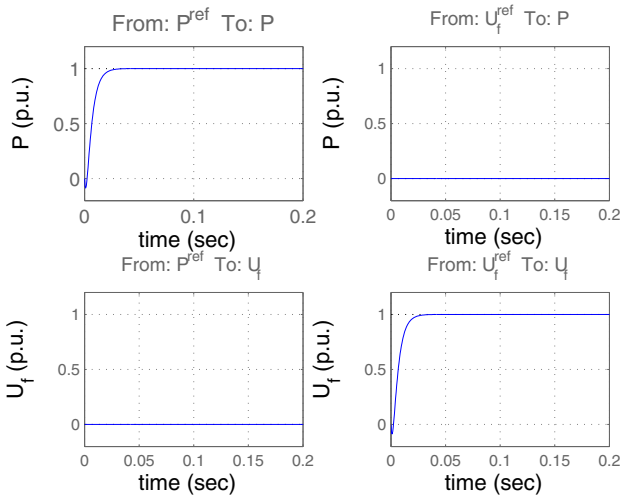

Fig. 6. Active-power and alternating-voltage step responses of the controller designed by IMC. Main circuit parameters: L_g=0.667 p.u. (SCR=1.5), R_g=0.01 p.u., L_c=0.2 p.u., R_c=0.01 p.u.. Initial conditions: V_0=1.05 p.u., E_0=1.0 p.u., θ_{v0}=56°. $H_{\mathrm{HP}}(s)$: k_v=0.35 p.u., α_v=40 rad/sec. IMC controller: α_p=200 rad/sec, α_u=200 rad/sec.

The IMC controller can easily be formulated in the classical feedback-control structure, as shown by the block diagram in Fig. 5. The controller $K'(s)$, therefore, can be written as

$$K'(s) = K(s)\left(I + \tilde{J}(s)\,K(s)\right)^{-1} \tag{24}$$

where I represents the identity matrix. Substituting (19) and (22) into (24) yields

$$K'(s) = \tilde{J}_n^{-1}(s)\,F(s)\left(I + \tilde{J}_p(s)\,F(s)\right)^{-1}. \tag{25}$$

B. Robustness with Model Variations

Due to its feedback-control nature, IMC is able to compensate for disturbances and model uncertainties. Consequently, the procedure of the IMC design is iterative. If the closed-loop performance is not satisfactory, the IMC controller has to be detuned (choosing lower bandwidths of $F(s)$) to ensure its robustness. In this section, the robustness of the multivariable IMC controller is demonstrated by a nonlinear VSC-HVDC model built in the PSCAD/EMTDC time-simulation software. The main circuits and control parameters are based on those that have been used in Fig. 6. The robustness of the controller is demonstrated with the variations in the following four categories:

- Ac capacitor sizes.

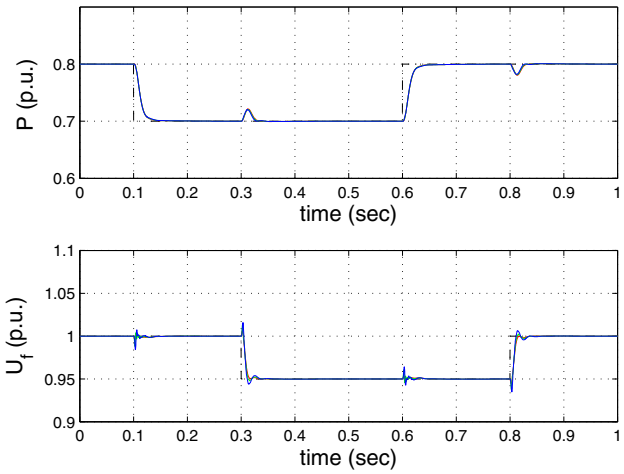

Fig. 7. Active-power and alternating-voltage step responses of the IMC controller with variations of ac capacitor sizes. Dashed: Reference signals, Red: C_f=0.0, Green: C_f=0.17 p.u., Blue: C_f=0.34 p.u..

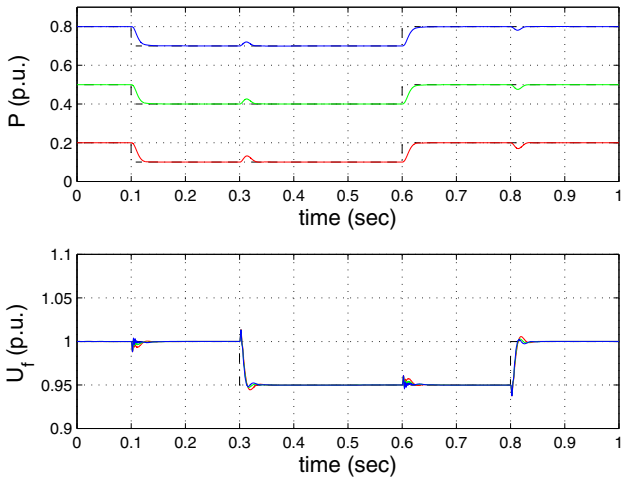

Fig. 8. Active-power and alternating-voltage step responses of the IMC controller with variations of power-transmission levels. Dashed: Reference signals, Red: P=0.2 p.u., Green: P=0.5 p.u., Blue: P=0.8 p.u..

- Power transmission levels.
- Ac system SCRs.
- Load disturbances.

Fig. 7 shows the active-power (0.1 sec and 0.6 sec) and alternating-voltage (0.3 sec and 0.8 sec) step responses when different sizes of ac capacitors are connected. It shows that the influence of the ac capacitor is minor, which justifies the design of the controller based on the reduced-order model. In the rest of the plots in this section, a normal-size ac capacitor ($C_f = 0.17$ p.u.) for VSC-HVDC is assumed.

Fig. 8 and 9 are the active-power and alternating-voltage step responses when the VSC-HVDC operates with different active-power levels and connects to ac systems with different SCRs. Fig. 9 shows a case with an ac-system strength of SCR $= 1.0$ (red curve), where fairly good performance has been achieved even though the VSC-HVDC is operating very close to the theoretical power-transmission limit.

Fig. 10 demonstrates the controller responses with different load disturbances. The tests are done by connecting a constant-power load P_L at the PCC at 0.1 sec and disconnecting it at 0.6 sec. The IMC controller shows good robustness when the alternating voltage is temporarily limited by the direct-voltage level ($P_L = 0.3$ p.u., blue curve).

IV. Multivariable $\mathcal{H}_\infty$ Control Design

$\mathcal{H}_\infty$ control is another methodology for MIMO controller design. The main feature of the $\mathcal{H}_\infty$ controller is its explicit way in dealing with model uncertainties, i.e., an $\mathcal{H}_\infty$ controller can achieve closed-loop stability with satisfactory performance under process variations as well as in the presence of other uncertainties such as disturbances and errors in the sensors.

Fig. 11 shows a standard multivariable feedback-control block diagram including process uncertainties. $\Delta_A(s)$ and $\Delta_M(s)$ represent the additive and multiplicative uncertainties respectively. The transfer matrices $S(s)$, $R(s)$ and $T(s)$ are

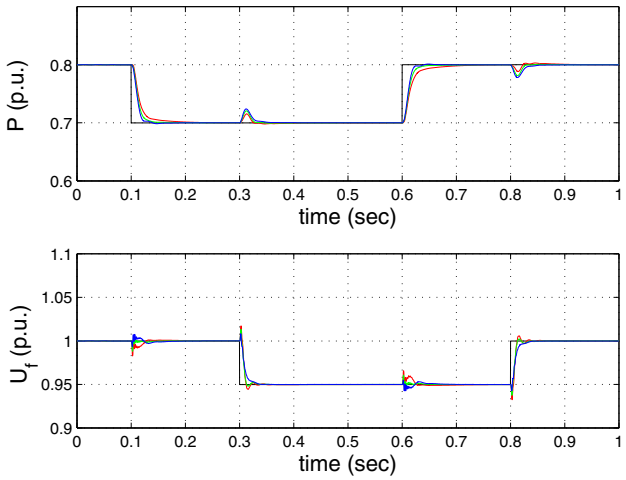

Fig. 9. Active-power and alternating-voltage step responses of the IMC controller with variations of SCRs of the ac system. Dashed: Reference signals, Red: SCR=1.0 p.u., Green: SCR=1.5 p.u., Blue: SCR=3.0 p.u..

defined as

$$\begin{aligned} S(s) &= (I + J(s)K(s))^{-1} \\ R(s) &= K(s)(I + J(s)K(s))^{-1} \\ T(s) &= J(s)K(s)(I + J(s)K(s))^{-1} \end{aligned} \tag{26}$$

where S and T are known as sensitivity and complementary sensitivity functions respectively. The matrix R does not have a name yet.

The singular values of the sensitivity function $\bar{\sigma}(S(j\omega))$ determine the disturbance attenuation, because $S(s)$ is in fact the closed-loop transfer function from disturbance to plant output. Thus, a disturbance attenuation performance specification can be written as

$$\bar{\sigma}(S(j\omega)) \leq |W_1^{-1}(j\omega)|. \tag{27}$$

Allowing $|W_1^{-1}(j\omega)|$ to depend on frequency ω enables to specify a different attenuation factor for each frequency ω. In

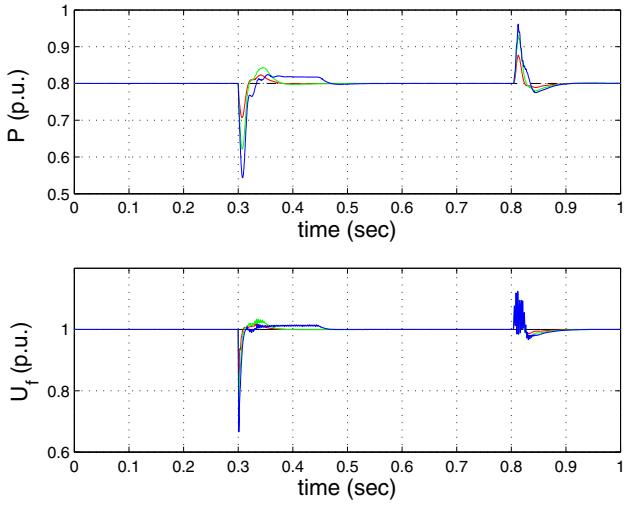

Fig. 10. Robustness of the IMC controller under load disturbances. Dashed: Reference signals, Red: $P_L = 0.1$ p.u., Green: $P_L = 0.2$ p.u., Blue: $P_L = 0.3$ p.u..

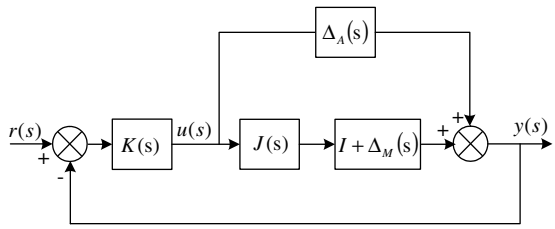

Fig. 11. Additive and multiplicative uncertainties.

$\mathcal{H}_\infty$ control, the performance can be achieved by finding the controller $K(s)$ through solving the problem

$$||W_1(j\omega) \cdot S(j\omega)||_\infty < \gamma \tag{28}$$

where ∞ denotes the infinite norm. The value γ is a constant which indicates the accuracy to which the optimal loop matches the desired loop shape.

The singular values of the complementary sensitivity function $\bar{\sigma}(T(j\omega))$ are used to measure the stability margins with respect to Δ_A and Δ_M, respectively, as shown in Fig. 11.

Assuming the additive uncertainty $\Delta_A(j\omega) = 0$, taking $\bar{\sigma}(\Delta_M(j\omega))$ to be the definition of the size of $\Delta_M(j\omega)$, the size of the smallest multiplicative destabilizing uncertainty $\Delta_M(j\omega)$ is

$$\bar{\sigma}(\Delta_M(j\omega)) = \frac{1}{\bar{\sigma}(T(j\omega))}. \tag{29}$$

The smaller is $\bar{\sigma}(T(j\omega))$, the greater will be the size of the smallest destabilizing multiplicative perturbation, and hence the greater will be the stability margin.

A similar result is available for relating the stability margin with respect to the additive plant perturbations

$$\bar{\sigma}(\Delta_A(j\omega)) = \frac{1}{\bar{\sigma}(R(j\omega))}. \tag{30}$$

As a consequence of (29) and (30), the stability margins of control systems are specified via singular-value inequalities such as

$$\begin{aligned} \bar{\sigma}(R(j\omega)) &\le |W_2^{-1}(j\omega)| \\ \bar{\sigma}(T(j\omega)) &\le |W_3^{-1}(j\omega)|. \end{aligned} \tag{31}$$

It is common practice to lump the effects of all plant uncertainties into a single fictitious multiplicative perturbation Δ_M, i.e., allowing $|W_3^{-1}(j\omega)|$ to depend on frequency ω to specify a different attenuation factor for each frequency ω. The stability margin can be achieved by finding the controller $K(s)$ through solving the problem

$$||W_3(j\omega) \cdot T(j\omega)||_\infty < \gamma. \tag{32}$$

In order to guarantee closed-loop stability and at the same time to achieve desired control performance under process uncertainties, the objectives of performance and robust stability can be simultaneously achieved by finding a controller $K(s)$ that satisfies both (28) and (32). The solution of the optimal problem is often called $\mathcal{H}_\infty$ controller based on mixed performance and robustness objectives. The numerical methods for solving $\mathcal{H}_\infty$ optimization problem are usually complex. Thus, commercial softwares, such as MATLAB, are commonly used to ease such tasks. The major work for the designer is then to specify $W_1(j\omega)$ and $W_3(j\omega)$ to meet the design requirement of the control performance and robustness.

Following the definition in (26), the sensitivity function S and complementary sensitivity function T have the relation

$$S(s) + T(s) = I \tag{33}$$

i.e., S and T cannot both be small at the same frequency. The relationship between S and T reflects the inherent conflict between control performance and robustness. Fortunately, this conflict can be resolved by requiring S to be small at low frequencies, and T to be small at high frequencies, due to the fact that the control performance is more important in the low-frequency range, while measurement noise and other plant uncertainties are often of high-frequency nature.

In $\mathcal{H}_\infty$ design, the closed-loop system performance is basically defined by $W_1(j\omega)$ and $W_3(j\omega)$. Optimization algorithms are used to synthesize the controller with the bandwidth between the crossover frequency of $W_1(j\omega)$ and $W_3(j\omega)$. Similar as the IMC design, the RHP zero has to be considered in determining the bandwidth of the closed-loop system, i.e., the desired bandwidth should be lower than half of the RHP-zero location. The basic principle for selecting weighting functions are to give $W_1(j\omega)$ a low-pass property and $W_3(j\omega)$ a high-pass property. It is necessary to ensure that the crossover frequency for the bode plot of $W_1(j\omega)$ is below the crossover frequency of $W_3(j\omega)$, such that there is a gap for the desired loop shape to pass.

Fig. 12 shows the Bode diagrams of $W_1(j\omega)$ and $W_3(j\omega)$, which have the following transfer functions

$$\begin{aligned} W_1(s) &= \frac{s/M + \omega_S}{s + A_S * \omega_S} \\ W_3(s) &= \frac{s + \omega_T/M}{A_T * s + \omega_T} \end{aligned} \tag{34}$$

where M represents the desired bounds on $||S||_\infty$ and $||T||_\infty$, A_S and A_T are the desired disturbance attenuation inside

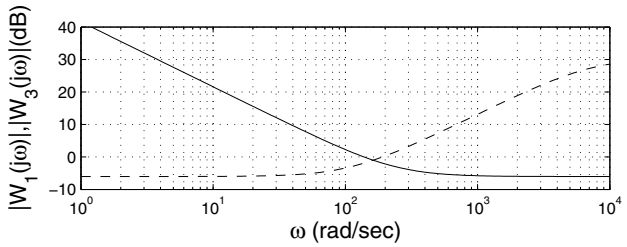

Fig. 12. Bode diagram (magnitude) of $W_1(j\omega)$ and $W_3(j\omega)$. Solid: $W_1(j\omega)$, Dashed: $W_3(j\omega)$. Parameters: $M = 2.0$, A_S=0.0002, A_T=0.03, $\omega_S = 120$ rad/sec, $\omega_T = 220$ rad/sec.

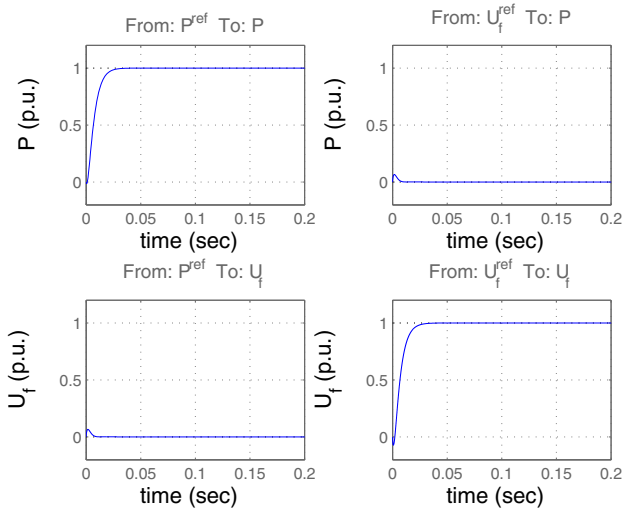

Fig. 13. Active-power and alternating-voltage step responses of the controller designed by $\mathcal{H}_\infty$. Main circuit parameters: L_g=0.667 p.u. (SCR=1.5), R_g=0.01 p.u., L_c=0.2 p.u., R_c=0.01 p.u.. Initial conditions: V_0=1.05 p.u., E_0=1.0 p.u., θ_{v0}=56°. $H_{\rm HP}(s)$: k_v=0.35 p.u., α_v=40 rad/sec. $\mathcal{H}_\infty$ controller: $M = 2.0$, A_S=0.0002, A_T=0.03, $\omega_S = 120$ rad/sec, $\omega_T = 220$ rad/sec.

bandwidth for S and T, and ω_S and ω_T are the crossover frequencies of W_1 and W_3 respectively.

As shown by the active-power and alternating-voltage step-responses in Fig. 13, the $\mathcal{H}_\infty$ controller also successfully decouples the cross-coupling between the two control channels. However, different from IMC, where a transparent algorithm was used, $\mathcal{H}_\infty$ control achieved the decoupling through optimization. Consequently, a slight cross-coupling can still be observed in Fig. 13. The control parameters have been chosen in such a way that the $\mathcal{H}_\infty$ controller has the same response time as the IMC controller to easily compare the results from the two controllers.

Fig. 14, 15, 16, and 17 show the results of the robustness tests for the $\mathcal{H}_\infty$ controller that correspond to the tests done for the IMC controller in Fig. 7, 8, 9, and 10. Generally speaking, both of the two control designs give good performance and robustness. While $\mathcal{H}_\infty$ shows slightly better robustness with ac-capacitor and power-level variations, the IMC controller shows better robustness with SCR variations and load disturbances. In addition, the IMC controller generally shows better agreement between the linear model and the nonlinear model than the $\mathcal{H}_\infty$ controller does.

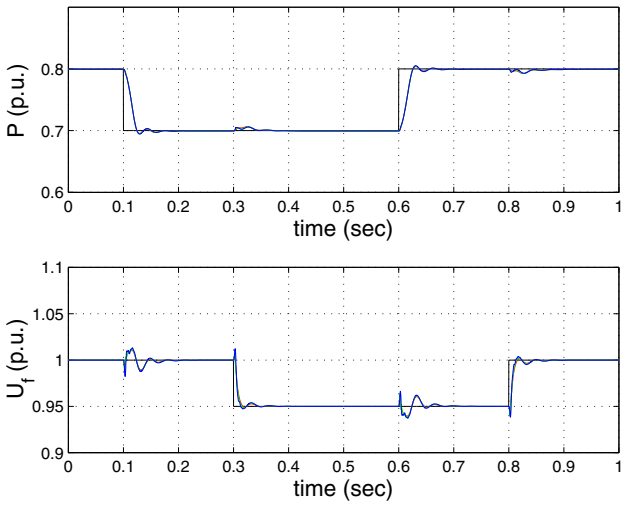

Fig. 14. Active-power and alternating-voltage step responses of the $\mathcal{H}_\infty$ controller with variations of ac-capacitor sizes. Dashed: Reference signals, Red: C_f=0.0, Green: C_f=0.17 p.u., Blue: C_f=0.34 p.u..

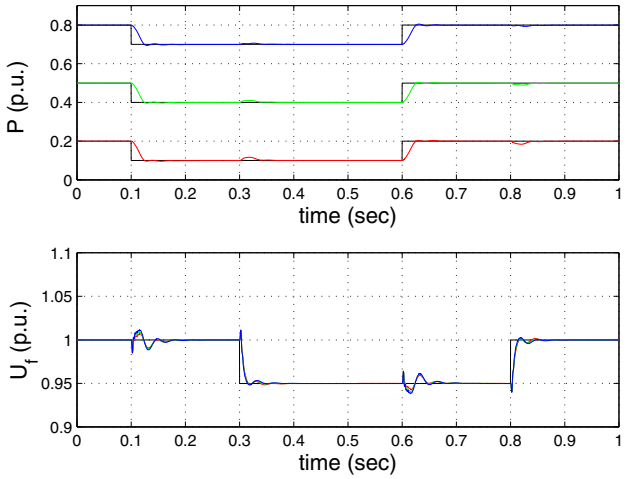

Fig. 15. Active-power and alternating-voltage step responses of the $\mathcal{H}_\infty$ controller with variations of power-transmission levels. Dashed: Reference signals, Red: $P = 0.2$ p.u., Green: P=0.5 p.u., Blue: $P = 0.8$ p.u..

V. Conclusions

In this paper, the multivariable feedback control aspect of the power-synchronization control for VSC-HVDC is investigated by two design approaches: IMC and $\mathcal{H}_\infty$ control. The algorithm used for the IMC design is simple and transparent, yet it achieves similar or even better control performance and robustness compared to the more advanced optimization-based $\mathcal{H}_\infty$ control. The investigation also shows:

- VSC-HVDC based on power-synchronization control is able to achieve good performance and robustness even in very weak ac-system connections.
- The cross-coupling between active-power and alternating-voltage control can be effectively decoupled by multivariable feedback design approaches.
- The high-pass current control effectively provides damping to the resonant poles. It is especially useful in weak ac-system connections where the low-order harmonic res-

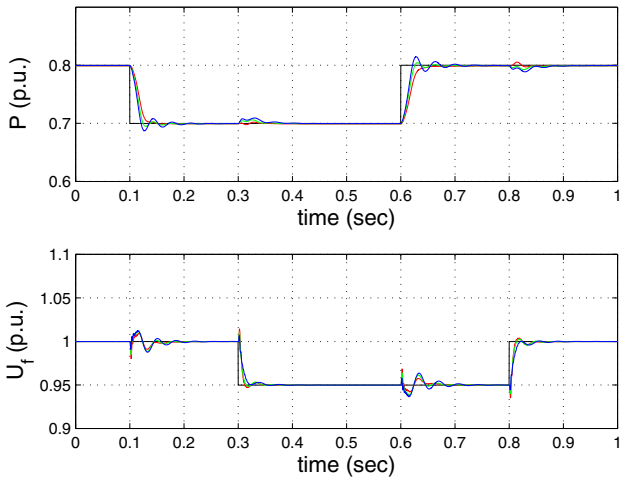

Fig. 16. Active-power and alternating-voltage step responses of the $\mathcal{H}_\infty$ controller with variations of SCRs of the ac system. Dashed: Reference signals, Red: SCR=1.0 p.u., Green: SCR=1.5 p.u., Blue: SCR=3.0 p.u..

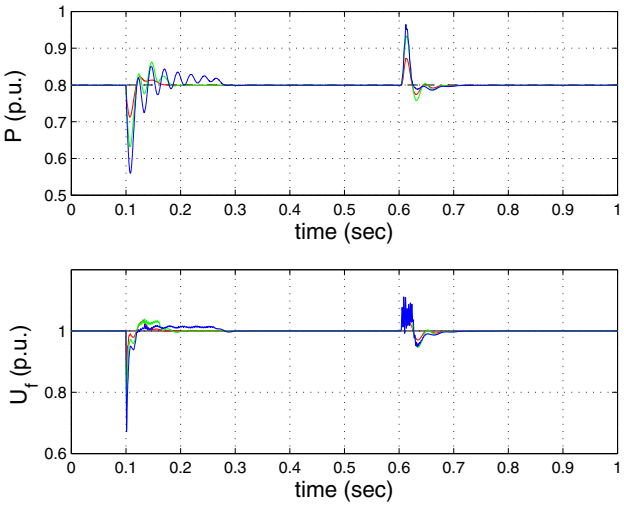

Fig. 17. Robustness of the $\mathcal{H}_\infty$ controller under load disturbances. Dashed: Reference signals, Red: $P_L = 0.1$ p.u., Green: $P_L = 0.2$ p.u., Blue: $P_L = 0.3$ p.u..

onance can otherwise interfere with the control systems of VSC-HVDC.

- The reduced-order system model can serve as a good base for the controller design, which results in lower-order controllers.

REFERENCES

[1] G. Asplund, K. Eriksson, and H. Jiang, "DC transmission based on voltage source converters," in *Cigre Conference 14-302*, France, 1998.

[2] A. Lindberg and L. Lindberg, "Inner current loop for large voltage source converters operating at low switching frequency," in *IEE Conference on Power Electronics and Variable-Speed Drives*, London, 1994.

[3] J. Svensson, "Inclusion of dead-time and parameter variations in vsc modeling for predicting responses of grid voltage harmonics," in *7th European Conference on Power Electronics and Applications (EPE'97)*, Trondheim, Norway, 1997.

[4] M. P. Kazmierkowski and L. Malesani, "Current control techniques for three-phase voltage-source PWM converters: A survey," *IEEE Trans. Ind. Electron.*, vol. 45, no. 5, pp. 691–703, 1998.

[5] M. Durrant, H. Werner, and K. Abbott, "Model of a VSC HVDC terminal attached to a weak ac system," in *IEEE Conference on Control Applications*, Istanbul, 2003.

[6] H. Konishi, C. Takahashi, H. Kishibe, and H. Sato, "A consideration of stable operating power limits in VSC-HVDC systems," in *Seventh International Conference on AC-DC Power Transmission*, London, 2001.

[7] L. Zhang, L. Harnefors, and H. Nee, "Power-synchronization control of grid-connected voltage-source converters," Submitted to *IEEE tran. on Power Syst.*

[8] L. Harnefors, M. Bongiornos, and S. Lundberg, "Input-admittance calculation and shaping for controlled voltage-source converters," *IEEE Trans. Ind. Electron.*, vol. 54, no. 6, pp. 3323–3334, Dec. 2007.

[9] D. Jovcic, L. Lamont, and L. Xu, "VSC transmission model for analytical studies," in *IEEE Power Engineering Society General Meeting*, Toronto, 2003.

[10] M. Morari and E. Zafiriou, *Robust Process Control*. Englewood Cliffs, New Jersey: Prentice-Hall, Inc., 1989.

[11] B. W. Bequette, *Process Control*. Upper Saddle River, NJ: Prentice-Hall, Inc., 2003.

[12] S. Skogestad and I. Postlethwaite, *Multivariable Feedback Control, 2nd Edition*. New York, NY: John Wiley & Sons Ltd., 2005.

Lidong Zhang (M'07) received the B.Sc. degree from the North China Electric Power University, Baoding, China, in 1991 and the Tech.Lic degree from Chalmers University of Technology, Gothenburg, Sweden, in 1999. From 1991 to 1996, he worked as an engineer with the Leda Electric co., Beijing, China. Since 1999, he has been with ABB Power Systems, Ludvika, Sweden. From 2007, he has been studying part time as an industrial Ph.D student in the Royal Institute of Technology, Stockholm, Sweden. His research interests are HVDC, power system stability and control, and power quality.

Hans-Peter Nee (S'91-M'96-SM'04) was born in 1963 in Västerås, Sweden. He received the M.Sc., Licentiate, and Ph.D degrees in electrical engineering from the Royal Institute of Technology, Stockholm, Sweden, in 1987, 1992, and 1996, respectively, where he in 1999 was appointed Professor of Power Electronics in the Department of Electrical Engineering. His interests are power electronic converters, semiconductor components and control aspects of utility applications, like FACTS and HVDC, and variable-speed drives. Prof. Nee was awarded the Energy Prize by the Swedish State Power Board in 1991, the ICEM'94 (Paris) Verbal Prize in 1994, the Torsten Lindström Electric Power Scholarship in 1996, and the Elforsk Scholarship in 1997. He has served in the board of the IEEE Sweden Section for many years and was the chairman of the board during 2002 and 2003. He is also a member of EPE and serves in the Executive Council and in the International Steering Committee. Additionally, Prof. Nee is active in IEC and the corresponding Swedish organization SEK in the committees TC 25 and TK 25 respectively.